

Developing an Automated Analysis for Proton Beam Monitoring

MPhys Semester One Project Report

Lewis Dean
Student ID: 10823674

Performed in collaboration with Robin de Freitas (10887826)

Supervisors: Prof. Cinzia Da Via and Prof. Stephen Watts

University of Manchester
Department of Physics and Astronomy
April 27, 2025

Abstract

The project we have been designated requires the development of a Graphical User Interface (GUI) through which one can image the scintillation light produced when a proton beam is made incident upon some scintillator. This semester, the focus has revolved around automating the method for determination of Bragg peak depths, that was devised prior to our project, in preparation for integration into our GUI. We have applied this updated analysis to the experimental data and compared the results to TOPAS simulations replicating the experimental setup. From these we have concluded, as was also suggested by a previous group of students, the beam energies inputted into our simulations are systematically higher than the energy of the Christie Hospital's proton beam when incident upon the scintillator. Notwithstanding this error, the automated analysis employed here is of comparable accuracy and precision to the original procedure, and this precision will be increased further when we can fully utilise our best calibrations.

1 Introduction

Within oncology, numerous methods can be employed to target the cancerous cells of patients. Some of the most common are chemotherapy, gene therapy and radiotherapy [1]. The latter can be further divided into either photon therapy or particle therapies like proton beam therapy (PBT). The energies of the X-rays/ γ -rays used in photon therapy decrease with the depth travelled into a patient's tissue; therefore, to deliver a significant dose to a tumour, the healthy tissue above must necessarily be damaged more-so, and further damage is done to healthy tissue beyond the tumour's depth. On the contrary, as heavy-charged particles, like protons, traverse a medium, the energy they deposit into said medium is governed by the Bethe-Bloch equation. That is, protons initially deposit minimal energy into the material, but their rate of energy deposition increases as they slow down. This rate of energy loss reaches a sharp maximum at the Bragg peak, occurring at a depth dependent upon the incident beam's energy, after which the protons come to near instantaneous rest. The clear benefit of this behaviour is that when administering PBT, the dose delivered to a patient's tissue can be localised to the tumour's neighbourhood by the appropriate choice of beam energy. For the reasons above, proton beam therapy, first proposed by Robert Wilson in 1946 [2], is considered one of the most viable methods of non-invasive cancer treatment.

This semester, my lab partner, Robin de Freitas, and I have built upon experiments contributed to by previous students and group members: these include Alf Phillips, Samuel Joughin, Jiayuan Feng, Prof. Stephen Watts and Mosst Tasnim Binte Shawkat. Their experiments aimed to quantify how successful a cost-effective piece of apparatus could be at imaging the light emitted by a scintillator upon interaction with a proton beam. These images were then analysed to determine the Bragg peak depths and mean ranges of protons of various energies. The experimental depths determined were compared to simulated Bragg peak depths and only the lower bound of simulated penetration depths deemed possible were consistent with the depths observed. This implied that some systematic error may have existed within their procedure. One goal of our project has been to address possible sources of this error, however our primary objective is to build a Graphical User Interface (GUI), associated with the apparatus designed by our group, through which a user can both calibrate the cameras and perform the full scintillation light analysis necessary for the determination of proton penetration depths. The core logic for the backend has been produced this semester, with the majority of frontend development left for Semester Two.

Unfortunately, we are yet to have visited the Christie Hospital ourselves to take our own beam images. Therefore, the scintillation light analysis discussed during this report makes uses of images taken last semester.

2 Proton Beam Preparation

The experiments performed by our group used Beamline A at the Christie Hospital. The therapeutic energies used within PBT are within the range 70-250 MeV [3]; protons are made to reach these kinetic energies by passing them through an isochronous cyclotron. Inside this cyclotron, a vertical magnetic field is applied, which imposes a Lorentz force upon the protons such that they are guided along a circular orbit. As they orbit, an electric field is applied parallel to their trajectory, accelerating them up to a maximum speed of $\sim 0.6c$. Upon reaching this maximum, they are made to exit the cyclotron by extraction magnets, after which they can be reduced to the desired therapeutic energy through interaction with an Energy Selection System (ESS). The ESS consists of carbon stepped degraders, wherein a step of a given thickness is introduced into the beam's path [3]. The expected number of proton interactions within the carbon define the expected energy that protons exit with.

The produced beam propagates through a vacuum, to maintain its energy, before it would be bent into one of three gantries if being used to treat patients, however any experiments are to be performed in the Stoller research room [3]. The beam is made to pass through a series of quadrupole magnets so as to focus the protons into a narrow "pencil" beam. The benefit of pencil proton beams in PBT, with their minimal width, is that, provided the beam can accurately target a tumour, the lateral dose to healthy tissue is minimised [4]. The focussed beam is delivered through a nozzle, which contains two orthogonal scanning magnets that steer the protons towards the target volume, i.e. towards a plastic scintillator in our case.

It is worth noting that settings such as the beam's energy, current, and the location in which the beam is focussed are controlled through a system designed by the company Varian [5], and hence by necessity will need to be handled outside of our GUI.

3 Plastic Scintillators and their Proton Interactions

First of all, we have access to the same plastic scintillator used in the experiments last semester. Based upon their measurement of the block's density, they determined the plastic was likely polystyrene. This impacted the refractive index they used for their optical corrections of observed scintillation light, as well as the scintillator material to be inputted to their Monte-Carlo simulations. However, having remeasured the density this semester as $1.035 \pm 0.03 \text{ g/cm}^3$, comparison to the Particle Data Group (PDG) signifies that the scintillator may actually be made of polyvinyltoluene (PVT), which has a density of 1.032 g/cm^3 [6]. The PDG reference provided quotes a refractive index of 1.58, but this is for Na D light specifically. Given that PVT is a dispersive medium, the refractive index considered in our analysis should match the wavelength of the scintillation light, hence an effective refractive index of 1.66 for PVT scintillators was to be used, as found within Nakamura et al [7].

Scintillators can be divided into two categories: organic and inorganic scintillators. PVT, being a type of plastic, is made into an organic scintillator by doping it with a fluorescent emitter. As charged particles, such as protons, enter the material, the dopant's electrons are excited, and their de-excitation results in the emission of scintillation light. A benefit of organic scintillators is that they are often cheaper than their inorganic counterparts, thus their use in these experiments aligns with the general desire for our setup to be cost-effective, hopefully encouraging other researchers to reproduce the apparatus.

In the introduction, I touched upon the Bethe-Bloch equation, which describes how the linear energy transfer (LET) from a heavy charged particle into a medium varies with that particle's energy. The derivation of this equation can be found in many textbooks, but here I refer to William Frass' lecture notes for a derivation [8]. In the data we have analysed, the beam energies are sufficiently low for this non-relativistic form to be appropriate, with the key result being that the energy lost per distance travelled by a heavy charged particle is inversely proportional to the square of its velocity. I.e,

$$-\frac{dE}{dx} \propto \frac{1}{v^2}. \quad (1)$$

The right-hand term has been coined the particle's stopping power, which is the negative of its associated LET. If the LET is plotted as a function of the depth traversed within the material, the resulting curve is known as its Bragg curve. It features a distinctive sharp peak, known as the Bragg peak, in which most of the particle's energy is deposited into the material. Example Bragg curves can be seen much later in the report within Figure 11b. The LET of the protons can ionise and/or excite electrons within the scintillator, meaning the LET distribution can be inferred from the intensity of scintillation light and thus the distribution of scintillation light distribution parallel to the beam's axis is an analogue of the Bragg curve. In 1996, Thomas Bortfeld devised an analytic approximation to the Bragg curve [9]; later during our analysis, we will fit this model to the observed on-axis scintillation light.

The preparation of the beam described in Section 2 leads to protons being Gaussianly distributed transverse to the beam's axis. As protons propagate through the PVT scintillator, they undergo multi-coulomb scattering (MCS) from nuclei; this is the accumulation of many small angle deviations in the trajectories of projectiles as they interact with charged particles within the material they are traversing. Such scattering is most accurately described by Molière theory however, for particles traversing thick materials like the scintillator here, Highland's formula for the root mean square scattering angle can be applied to simplify the treatment [10]. Crucially, the contributions from a vast number of independent scattering events means the total scatter satisfies the central limit theorem, and thus the beam's transverse distribution remains Gaussian, although MCS causes its width to broaden with penetration depth. This broadening is seen most prominently in the vicinity of the Bragg peak depth; the protons in this region have slowed and are thus more susceptible to larger scattering angles, resulting in a sudden increase in the beam's lateral penumbra about the Bragg peak.

Furthermore, the focussing of the beam by quadrupole magnets is used to position the beam's focus inside of the scintillator. Therefore, the broadening of the Gaussian is increased/decreased depending on whether the beam is converging prior to the focus or diverging after it. The net effect of these factors is that the intensity of scintillation light must also follow a Gaussian distribution perpendicular to the beam axis. This justifies the approach taken in the updated analysis procedure as described in Section 7.

4 Experimental Apparatus

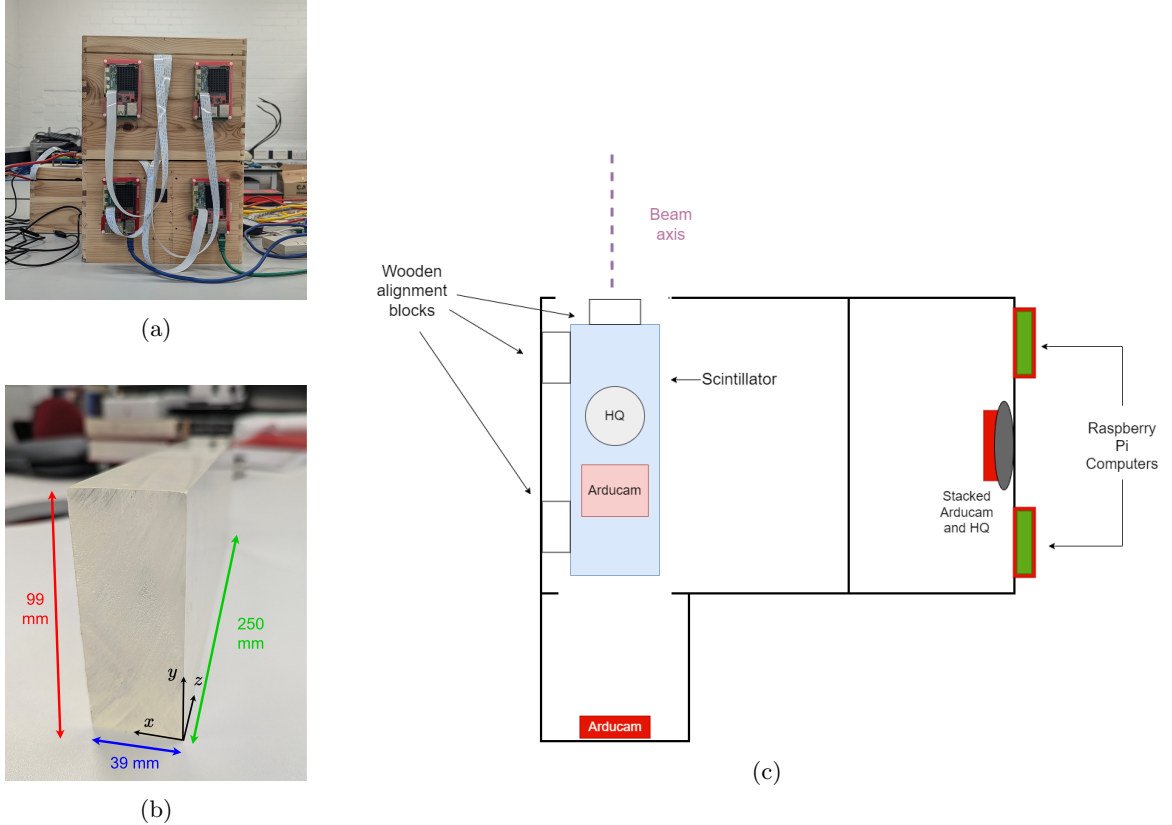


Figure 1: (a) Wooden box that houses the scintillator, with the mounted Raspberry Pi computers visible. (b) PVT scintillator's rough face, with the block's dimensions and the origin associated with the box's coordinate system annotated. Note the error on the (x , y , z) block dimensions are (0.1, 0.1, 0.5) mm respectively. (c) Top-down schematic of the apparatus when the box's lid is removed. The five cameras (HQ or Arducam) are shown, with the two positioned on the scintillator actually mounted inside the lid.

The experimental setup used for imaging scintillation light, designed prior to our project, is illustrated in Figure 1. The wooden box was constructed to house the scintillator, shielding it from external light during a beam run, whilst also allowing Raspberry Pi camera modules to be mounted inside at fixed positions relative to the scintillator. To ensure the scintillator position is invariant, three wooden blocks have been screwed into the base of the box which the scintillator gets pressed against when placed inside. The interior of the box is painted black, in a bid to reduce the reflection of any scintillation light. In total, five Raspberry Pis computers are mounted to the exterior of the box with stand-offs; two are connected to cameras imaging the side face of the scintillator, two for imaging its top face, and one Pi is connected to an on-axis camera. Later in the report, it will become clear why imaging multiple perspectives of the same event is essential to our analysis.

Two types of camera are used within these experiments: three Raspberry Pi IMX477 HQ cameras and two Arducam IMX519 Autofocus cameras. The on-axis camera is Arducam, whilst the top/side perspectives of the scintillator are imaged by Arducam-HQ pairs. Unfortunately, during the experiments

performed on the 9th of April 2024, the top Arducam camera was unable to focus. As a result, we could not use any of its data in our analyses. It seems that a software update managed to resolve this issue, meaning it is now operational for the experiments we perform in Semester Two.

Performance Metric	IMX477 HQ	Arducam IMX519
Sensor Resolution	4056×3040	4656×3496
Focus Adjustment	Manually adjusted by hand with focus ring	Autofocus mode or remote manual adjustment
Optical Size	$1/2.3''$	$1/2.53''$
Distortion	Notable barrel distortion	No distortion visible by eye

Table 1: Comparison of the two camera types used: the Raspberry Pi IMX477 HQ and Arducam IMX519 cameras. These specs were sourced from the Arducam website [11].

The comparison made in Table 1 intends to quantify the advantages offered by each type of camera. The higher resolution of the Arducam allows sources of scintillation light to be defined more precisely, whereas its lower optical size compared to the HQ camera means that it can capture slightly less light and offers a slightly smaller field-of-view (FOV). That being said, the full scintillator is within the Arducam FOV and, if light distributions are to be averaged over multiple images, reduced light collection is not an issue. In the spirit of reproducibility, the Arducam’s ability to have the camera focus set through some command parameter, rather than by hand, means we can be more confident that any previously optimised focus settings can be re-implemented at a later date. Another big drawback of the HQ cameras are their significant barrel distortion which requires correction. For these reasons, the Arducam is deemed the superior camera. Inevitably, we needed to calibrate both camera types because we only have the existing images and, since the top Arducam was unable to focus, our only top face perspective of the scintillation light is through a HQ camera.

Originally, the scintillator was too long to fully fit within the box. Therefore, they had the scintillator’s length cut down. Doing so introduced a rough face which cannot not be easily smoothed. Considering this, the scintillator will always orientated such that proton beams enter via the rough face. This is deemed more appropriate than having the on-axis camera image the rough face, since the scintillation light refracting out of said face would be diffuse, leading to blurry images.

5 Software GUI

As discussed earlier, the previous group of students showed this setup’s potential for the determination of Bragg peak depths. Their analysis of the images was relatively simple, however it required plenty of manual input to execute. Imaging for a given beam run involved using the software RealVNC to remotely access a “Master” Raspberry Pi; this then executed a Bash script which communicated the necessary image-taking commands with the other Pis via a Secure Shell (SSH). The images taken by each were then transferred back to the local device using the software WinSCP [12].

To avoid saturated images for a given beam energy, they performed test runs wherein images were taken with various analogue gains. The test images were inputted into the image processing software ImageJ, and the optimum gain was determined through the manual inspection of beam intensity profiles. After image-taking, when extracting a Bragg peak depth, the brightest pixel needed to have its corresponding physical position read off from a calibration image, which consisted of a ruler attached to the face of the scintillator being seen by the camera. Later, the images were corrected for distortion in another piece of software called PhotoPad [12].

As you can see, the existing data analysis procedure, being split across multiple pieces of software, had fundamental restrictions to its automation. For these reasons, a large part of this semester has involved redesigning the image analysis procedure to resolve this issue, as detailed in Section 6 and beyond. As a

result, development of the GUI, which was initially the key goal for the project, needed to be postponed until Semester Two.

5.1 GUI Prototype

Thus far, we have a primitive GUI with limited functionality, which I built over the first few weeks prior to the pivot towards exclusively refining the analysis procedure. Some screenshots of its features are depicted in Figure 2. The backend logic for the site is built with the web framework FastAPI. Currently, the user creates a JSON configuration file, consisting of the username, hostname, and password of each Raspberry Pi they wish to connect to. On the homepage, a button can be pressed that attempts to establish SSH connections with each of the configured Pis, requiring both the local device and Pis to be connected to the router with Ethernet cables.

From here, hyperlinks can direct the user to endpoints such as “Take Images”. This page features a checkbox list of the connected Pis so that a subset of cameras can be selected to take images. To ensure these images are taken simultaneously, the libcamera commands to be sent over SSH are executed concurrently. Note that all images taken through the GUI have timestamps within their filenames, and they can be accessed inside the interface on the “View Images” page. Finally, each Raspberry Pi can have a UDP stream of its camera feed viewed from within the GUI. This functionality is useful for when manually focussing the HQ cameras. Moreover, the stream snapshot button will be essential next semester when users are taking calibration images inside the GUI; the user can continually check the positioning of calibration patterns within a camera’s FOV before taking an image.

No calibration/data analysis pipelines are built into the GUI currently. This will be the next phase of GUI development, and a discussion of additional automation to be incorporated into our procedure is given in Section 9.

6 Updated Image Analysis

6.1 Camera calibration

A key improvement required to the previous method was the pixel-to-length conversion process. The need to compare back to an image of a calibration ruler restricts any potential automation. After some research, we realised that plane-to-plane homographies associated with the images taken by different cameras would, with further analysis, allow the 3D reconstruction of events/trajectories within a calibrated region of physical space. A plane-to-plane homography allows for the projection of a (real) world plane onto the image plane of the camera, or vice versa. Robin printed various calibration patterns to test from *calib.io* [13], namely chessboard patterns of various dimensions/tile sizes. Example chessboard patterns can be seen in Figures 3a and 3b.

The convention was made to define the top left chessboard corner, as seen through the camera, as the origin of each calibration plane’s coordinates. Given the uniform spacing of the chessboard corners, we know the physical position of each; the homography needs to map from the pixel containing that corner to its physical position. Using the Python computer vision library OpenCV, the array of chessboard corners can be identified and then the homography from the calibration world plane to the camera’s image plane can be built. Crucially, the inverse mapping determines the physical position upon the world plane associated with an inputted pixel. The latter will be used to make spatial measurements in the absence of the previously used reference calibration image.

When the 2D image points are expressed as 3D homogenous coordinates, the projection between planes can be modelled as a matrix transformation. In reflection of the notation used in Criminisi et al [14], the mapping from the image plane to a given world plane is given by,

$$\mathbf{X} = \mathcal{H}\mathbf{x}, \quad (2)$$

where \mathbf{X} is a homogenous position vector on the world plane, \mathbf{x} is that on the image plane, and \mathcal{H} is the (homogenous) homography matrix. Suppose n chessboard corners are used to build the homography. If

Proton Beam Imaging Software

The hostname for the local device is LewisPC.

[Click to connect with SSH](#)

SSH Connection Statuses

- o raspi5 - disconnected
- o c09796mb - disconnected
- o raspib2 - disconnected
- o raspib3 - disconnected

To add new Raspberry Pis to this list, edit the `raspberry_pi.json` setup file in the software repository.

[Stream Video](#)
[Take Images](#)
[View Images](#)

(a)



(b)

Raw Pi Images

[Take Images](#)
[Home Page](#)

[2024-10-22_16h-44m-51s_c09796mb_test.jpeg](#)



[2024-10-22_16h-43m-18s_raspib2_test.jpeg](#)



[2024-10-22_16h-34m-16s_raspib3_stream_snapshot.jpeg](#)



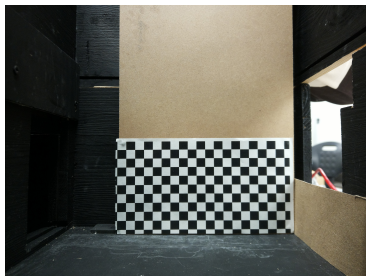
[2024-10-22_16h-31m-10s_raspib3_stream_snapshot.jpeg](#)

(c)

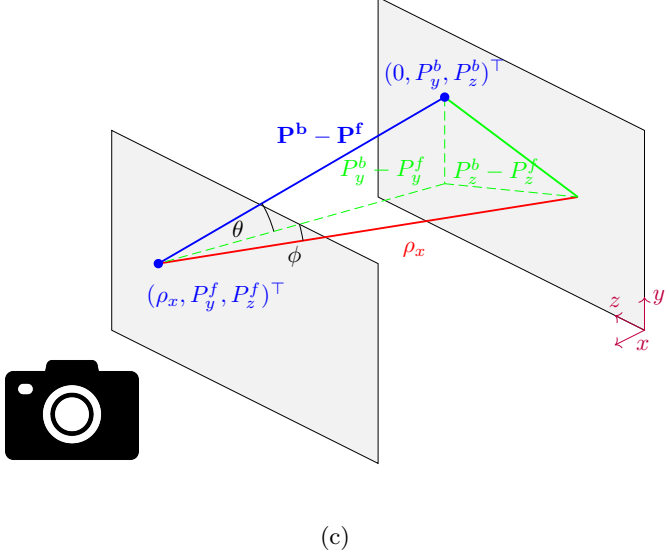
Figure 2: Screenshots of the primitive GUI made this semester. (a) Homepage. (b) Top HQ camera example for accessing a video stream of its camera feed. (c) Page for viewing the unprocessed (raw) images taken through the GUI.



(a)



(b)



(c)

Figure 3: (a) and (b) show example front/back plane calibration images for the side Arducam camera. (c) Diagram of the side camera perspective for showing how the angles (associated with the physical line interpolated for a given pixel) subtend from the optical axis. These angles are inferred through the difference in physical position when that single pixel is projected onto two different world planes. The points \mathbf{P}^f and \mathbf{P}^b represent the physical positions when projected onto the front and back planes respectively, and those planes are separated by a distance ρ_x .

\mathcal{H} has its elements collapsed into a vector, \mathbf{h} , then one can cast n relations of the form in equation 2 into the matrix equation,

$$A\mathbf{h} = \mathbf{0}, \quad (3)$$

in which A is a $2n \times 9$ matrix [14]. We want to estimate \mathbf{h} by finding that which minimises the residuals of $|A\mathbf{h}|$ [14]. I.e., by finding the \mathbf{h} which most closely satisfies equation 3. The size of these minimised residuals characterises the error associated with the estimated homography.

6.1.1 Errors on Homographies

It was Robin who produced the code that calculates the error associated with each homography projection. The procedure for doing so is beyond the scope of this report, but the process is outlined in Chapter 4 of Hartley and Zisserman’s book, Multiple View Geometry in Computer Vision [15]. Importantly, error arises from the precision to which the positions used to estimate the homography are known (the chessboard corner positions), as well as the number of points provided to help in estimation. Additionally, the identification of the pixel containing a point-of-interest may not always be exact; therefore, there will be uncertainty in the pixel (image coordinate) we want to project into a real world position.

6.2 Distortion Correction

As mentioned, the HQ cameras have notable barrel distortion. Given that the scintillation light analysis requires undistorted images, a procedure for distortion correction was employed. For a camera to be corrected, around 15-20 images were taken of a chessboard calibration board, with each image capturing the pattern within a different region of its field-of-view. The printed chessboard had tiles of side length 10 mm and we ensured calibration patterns were printed reliably by cross-checking them with digital calipers. Such a reference image set is sufficient to use OpenCV’s method of undistortion and rectification, which is applied within our image processing pipeline prior to any analyses.

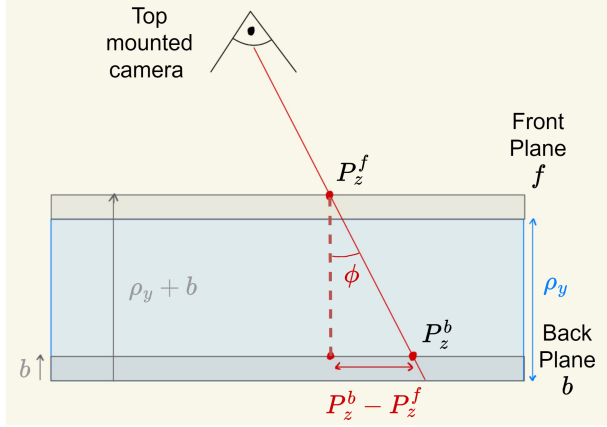


Figure 4: An example diagram for the top camera perspective as for why the finite thickness of the calibration boards must be factored into the line intersection method. Note b here represents the thickness of the board.

6.3 Line Intersection Method for 3D Pinpointing

For a given camera, a chessboard pattern is taped to a rigid board for use in two calibration images. The board is placed at different depths along the optical axis, so as to enclose the volume in which the scintillator will occupy inside the box. From these, two homographies can be built for those world planes which are herein referred to as the front and back planes, as would be seen through the camera. Now, consider a given pixel within an image taken by the camera; we can ask if the imaged event/point of interest is physically located on the front or back world plane, what physical position would their homographies map the pixel onto. These will be notated as \mathbf{P}^f and \mathbf{P}^b for the front and back planes respectively, and are illustrated as the blue points lying on each plane within Figure 3c. The variation in non-optical-axis coordinates comes from the depth perception effect in which objects further away occupy less space within the camera's field of view (i.e. the length per unit pixel increases with distance along the optical axis).

Using the side camera perspective as an example, one can use trigonometry to show,

$$\tan \phi = \frac{P_z^b - P_z^f}{\rho_x}, \quad (4a)$$

$$\tan \theta = \frac{P_y^b - P_y^f}{\rho_x}. \quad (4b)$$

where the labelling of components reflects the fact the side camera sees yz planes relative to the box's coordinate system (see Figure 1b for a reminder of the latter). Note that ρ_i refers to the i -directed depth between calibration planes, which crucially equals the scintillator's length along the i -axis. The angles ϕ and θ are defined in Figure 3c. Calibration plane coordinates will need to be transformed to the box's coordinate system. This depends upon the camera perspective and the positioning of the calibrated world planes, as well as additional shifts introduced due to the distance between the edge of the calibration board and the defined origin of the calibration patterns. Moreover, the finite thickness of the calibration boards needs accounting when transforming the in-plane coordinates. Using the top camera perspective as an example, Figure 4 indicates that after the transformation to the box's coordinates, the y components of the front and back plane positions would only be ρ_y and 0 respectively if the calibration board used had zero thickness. In reality, these components are $\rho_y + b$ and b , where b is the thickness of the board.

Once the two physical positions are in terms of the box coordinates, and the angles ϕ and θ have been calculated, one can build a vector equation between them, parameterising an interpolated line through physical space in which the real event must lie upon given the pixel it occupies. In accordance with Figure 3c's notation, the angles ϕ and θ per camera are used to label the angles inferred from the "horizontal" and "vertical" position displacement between the front and back plane projections respectively. That is,

horizontal and vertical as would be seen in the image plane. The full set of derived line equations for our box's coordinate system is,

$$\text{Side Camera : } \mathbf{P}(\lambda) = \left(0, P_y^b, P_z^b\right)^\top + \lambda \left(1, \tan \theta_{yz}, \tan \phi_{yz}\right)^\top, \quad (5a)$$

$$\text{Top Camera : } \mathbf{P}(\mu) = \left(P_x^b, 0, P_z^b\right)^\top + \mu \left(\tan \theta_{xz}, 1, \tan \phi_{xz}\right)^\top, \quad (5b)$$

$$\text{On-Axis Camera : } \mathbf{P}(\nu) = \left(P_x^b, P_y^b, 0\right)^\top + \nu \left(\tan \phi_{xy}, \tan \theta_{xy}, 1\right)^\top, \quad (5c)$$

in which the points chosen to parametrise the lines lie on the back calibration planes. The ij subscript notation for the angles specify the planes seen by the equation's associated camera. E.g., the on-axis camera sees xy planes.

If the same point of interest (POI) can be confidently identified from a second camera perspective, then a second interpolated line of possible physical positions can be constructed with its front/back plane homographies. If POI identification from each perspective could be specified with perfect sub-pixel precision then, given that the light rays arriving at the cameras emanate from the same 3D position, the interpolated line equations would uniquely intersect at the POI. In practice, due to the errors introduced by our implementation, the interpolated lines will actually be skew. For two arbitrary skew lines, $\mathbf{U}(\mu)$ and $\mathbf{V}(\nu)$, the distance of closest approach, D , is given by,

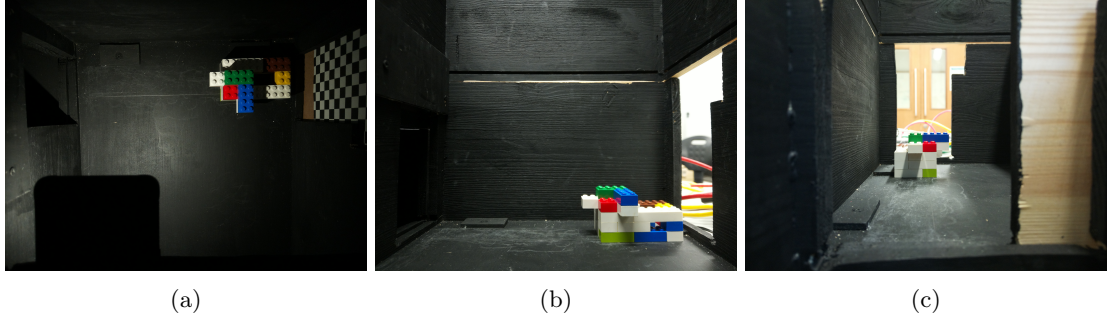
$$\begin{aligned} \mathbf{U}(\mu) &= \mathbf{U}_0 + \mu \mathbf{d}_U, \\ \mathbf{V}(\nu) &= \mathbf{V}_0 + \nu \mathbf{d}_V, \\ D &= \frac{\|(\mathbf{V}_0 - \mathbf{U}_0) \cdot (\mathbf{d}_U \times \mathbf{d}_V)\|}{\|\mathbf{d}_U \times \mathbf{d}_V\|}. \end{aligned} \quad (6)$$

where \mathbf{U}_0 and \mathbf{V}_0 are points upon $\mathbf{U}(\mu)$ and $\mathbf{V}(\nu)$ respectively, with \mathbf{d}_U and \mathbf{d}_V as each line's respective directional vectors. The condition for intersection we define is whether the "residual" distance of closest approach between the two lines is within 5 standard deviations of the total error between the 3D positions of each line's closest points. Of course, this is a rather relaxed condition; it aims to flag the case in which some significant failure in implementation exists. If the condition is satisfied, the "intersection" point is defined as the midpoint between the closest points of the lines. Note that this general approach to 3D pinpointing will often be called the "line intersection method" in subsequent sections.

The error in physical positions determined for each calibration plane was computed through the component-wise addition in quadrature of the error introduced by homography and that introduced by the shift between coordinate systems. Through standard methods, these were propagated through to errors on θ and ϕ and hence the vector line equations in 5a , 5b, and 5c. From the latter, the error on the closest points between two interpolated lines can be calculated and, if the intersection condition is met, propagated onto the error in the midpoint between those closest points. The significance of each error source to our final results is expanded upon in Section 8.2.

6.3.1 Testing the Line Intersection Method

We performed numerous investigations into the validity of both our homographies and the line intersection method. The culmination of these led me to build a small Lego structure, to be placed within the calibrated volume, in an attempt to pinpoint the physical position of a Lego brick corner. Lego was used due to the low tolerances on brick dimensions [16]. Additionally, the structure's sharply defined edges meant that images taken from the side, top, and on-axis perspectives could all have the pixel containing the corner identified with reasonable precision. Figure 5 shows the three images associated with each of the aforementioned perspectives, with the red brick's outmost corner being that pinpointed. For a given image, a Python script was used to overlay a small rectangle upon it; by trial and error, the size and centre position of this rectangle would be moved until it had side lengths the size of a few pixels and we could confidently say that the pixel containing the brick's corner lied somewhere inside of it. The



(a)

(b)

(c)

Figure 5: (a) Top camera (b) side camera (c) on-axis camera perspectives of the Lego structure placed inside the volume calibrated for the line intersection method. The side and on-axis images are rotated for clarity as these are taken 'upside-down' by default.

dimensions of the rectangle defined the uncertainty on the corner's pixel identification to be used when computing the error on the homographies.

With the images taken, three possible camera pairings can be made. The line intersection method was performed with each pair so that a weighted 3D point and its uncertainty could be calculated. The results of this are shown in Table 2, from which it can be seen that the method devised is consistent with that expected from the quoted Lego dimensions [17]. We took this result as evidence that we could move onto the next stage of length calibration, wherein the refraction of scintillation light through the scintillator would need to be built into the model.

Measurement Type	(x, y, z) position (mm)	Uncertainty in position (mm)
Using Lego dimensions	(47.6, 38.4, 79.4)	Negligible (tolerance ~ 0.01 mm)
Weighted intersection method	(47.3, 37.6, 79.7)	$\pm (0.5, 0.3, 0.4)$
Residual between methods	(0.3, 0.8, 0.3)	

Table 2: Comparison of the position determined for the red Lego corner, as seen in Figure 5, when the quoted Lego dimensions are used or the method for weighted 3D pinpointing is applied. The residuals and the errors on the line intersection method here shows that all coordinate components are consistent with the position expected from the Lego brick dimensions.

6.3.2 3D Pinpointing inside Scintillator

The method described thus far would not generalise to the case in which the scintillator is placed inside the calibrated region; the change in refractive index at the air-PVT boundary means that the direction vectors of the interpolated lines need modifying. We can calculate the angles ϕ and θ as before, as if the scintillator was not present, which represent the angles relative to the surface's normal in which light rays exit. These angles can be converted into the corresponding angles inside the scintillator via Snell's law, which can then be used to define the direction vectors of interpolated lines within the scintillator. An additional amendment is that the point parameterising the line now must lie on the front face (as seen by the relevant camera) of the scintillator, where previously the parameterising points in equations 5 had lied on the back calibration plane.

7 Christie Data Analysis

As mentioned, we are making use of images taken last semester, but our development of the line intersection method, which allows length calibration to be automated, unlocks areas of image analysis that were previously inaccessible. The intermediate results of our updated procedure will be outlined here for the 150 MeV proton beam run, however the final Bragg peak depths for the {130, 160, 170, 180}

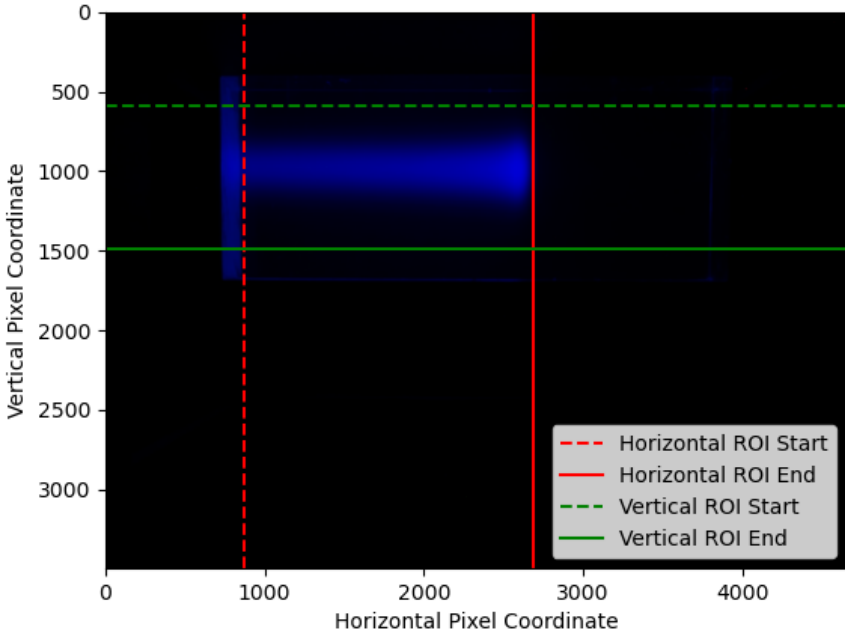


Figure 6: An example image of the scintillator during the 150 MeV beam run, produced by averaging many images taken from the side Arducam camera. The contours overlaid show the Region-Of-Interest (ROI) which was manually determined per averaged image.

MeV beam runs will also be presented later. Despite images being taken by four cameras per beam run, we have only used those by the side-mounted Arducam camera and the top-mounted HQ camera. We acknowledge the potential for increased precision if instead weighted average results from several camera pairings are calculated.

Figure 6 shows an example of the scintillation light observed during the 150 MeV beam run by the side-mounted Arducam camera. For images taken by a HQ camera, their barrel distortion is corrected, and the same distortion correction is applied to their calibration images prior to any homography building. Per beam run, dozens of images were taken per camera; the pixel brightness values across these images could be averaged to produce an image less susceptible to digital noise or scintillation light variation due to range-straggling. Each pixel within an image can be treated as a bin within a 2D histogram in which the pixel brightness, up to the application of an analogue gain scale factor, represents the number of scintillation photons being counted within the camera sensor region associated with the pixel. Therefore, given that the count within a histogram bin can be taken as a Poisson random variable, the uncertainty on the average pixel brightness, $\bar{\beta}$, is given by,

$$\Delta\bar{\beta} = \sqrt{\frac{\bar{\beta}}{N}}, \quad (7)$$

where N is the number of images being averaged over. Within the averaged image, only light emanating from within the scintillator is relevant to our analysis, thus a subregion of the image spanned by the scintillator needs identifying. I experimented with the automated edge detection using the OpenCV's implementation of the Canny algorithm. This could reliably extract the edges of the scintillator, however the Region-Of-Interest (ROI) is more subtle than this; as can be seen in Figure 6, the rightmost ROI edge must come closely after the maximum range of the protons, making it a function of beam energy, and a margin of error must be added to the leftmost ROI edge to neglect the region in which brightness is anomalously high due to light reflections from the anterior face. With the limited time this semester, I settled on the manual input of the ROI per camera per beam energy.

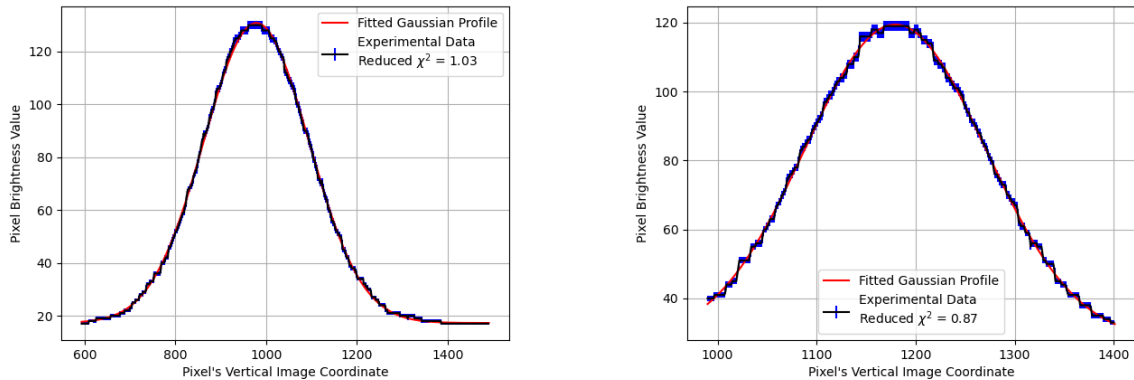
The averaged image is composed of three colour channels. Our analysis is applied to the blue channel as one can clearly see this channel dominates. We experimented with an analysis of a greyscale ver-

sion of the images, however the low amount of red and green light made their respective channels noisy, and introducing said noise made the greyscale image a worse candidate for analysis than the blue channel.

The identified ROI can be decomposed into columns of pixels positioned a given number of horizontal pixels across the image. Before image taking, green LAP lasers [3] were used to align the beam for normal incidence upon the scintillator's anterior face. If we naively assume this step was implemented perfectly, the beam axis would follow a horizontal straight line across the image, meaning the brightness across a given column of pixels would be Gaussian distributed. Therefore, we can fit Gaussian distributions to each pixel column within ROI. Initially, this is a 3-parameter fit, in which the Gaussian centre, scale, and width are variable, yet the background brightness level used is a hardcoded estimate. After this, fitting is repeated with background brightness introduced as a free parameter, and the fit parameters of the previous fitting round are passed as initial parameter estimates. This two-stage approach resulted in more reliable fit convergence across the full ROI.

Figures 7a and 7b show the fitted Gaussians, for the columns of pixels giving the lowest reduced χ^2 values, for the side Arducam and top HQ cameras respectively during the 150 MeV beam run. These reduced χ^2 values were calculated by ordinary Least Squares fits to the observed pixel brightness values. The largest reduced χ^2 for this beam run was from the top camera perspective and had a value of 72. Crucially, the fitted Gaussian centre position was still appropriate, but plotting this distribution reveals notably noisier Gaussian tails compared to those seen in Figure 7. Hence, a poorer fit is to be expected.

It is worth mentioning that, despite runs being taken with beam energies between 70-180 MeV, only the 130-180 MeV runs were compatible with the method we have implemented this semester. Last semester, the students performed test runs, as described in Section 5, so as to determine an optimum analogue gain for each beam energy. However, they did not appreciate that both the gain and exposure time contribute to the brightness of the images; the test runs used a higher frame rate (lower exposure time) than the main beam run. Thus, given that the test runs were used to determine a highest possible gain without saturation, the longer exposure time in the main run often led to saturated images. This manifests as a truncated Bragg peak intensity, which leads to the Gaussian fitting procedure failing in that region of these images. That being said, it is possible that by omission of saturated data from the Gaussian fitting process, reasonable fits could be achieved. We decided the modification of our method to accommodate saturated data was not necessary since, now we are aware of its origin in the images, we can more carefully prevent it when taking our own images next semester.



(a) The best fitted Gaussian along the ROI being scanned, during the 150 Mev beam run, from the side camera perspective. The fit has a reduced χ^2 of 1.03.

(b) The best fitted Gaussian along the ROI being scanned, during the 150 Mev beam run, from the top camera perspective. The fit has a reduced χ^2 of 0.87.

Figure 7

7.1 Incident Beam Angle Correction

Now, we track the change in vertical pixel coordinate containing the fitted Gaussian centre as a function of horizontal pixels across the ROI. Least squares linear regressions were fitted to these relationships and plotted as shown in Figures 8a and 8b for the side Arducam and top HQ images respectively. The error on each vertical beam centre coordinate was extracted from their associated Gaussian fits. Each plot's gradient is $\tan \alpha$, where α is the beam's angle as seen within that camera's image plane. For the 150 MeV beam run, the side and top cameras saw beam angles of $0.7677 \pm 0.0007^\circ$ and $1.6 \pm 0.001^\circ$ respectively.

For the high number of degrees of freedom involved in these fits, the reduced χ^2 values are too large, indicating some flaw in the methodology here. The presence of non-zero incident angles are clearly evident from the plots however. Given this, the Gaussians associated with each point on the plot were actually being fitted to skewed Gaussian distributions, since sampling pixel brightness values from vertical pixel columns is not yet perpendicular to the beam. Moreover, given the age of the scintillator, impurities developed over time may fragment the expected scintillation light distribution, and hence the uncertainty on pixel brightness estimated through merely the Poissonian approach may not suffice. That being said, this approach to determining the deviation from normal incidence was the best we identified, and the following amendment, although not perfect, does improve the accuracy of our analysis.

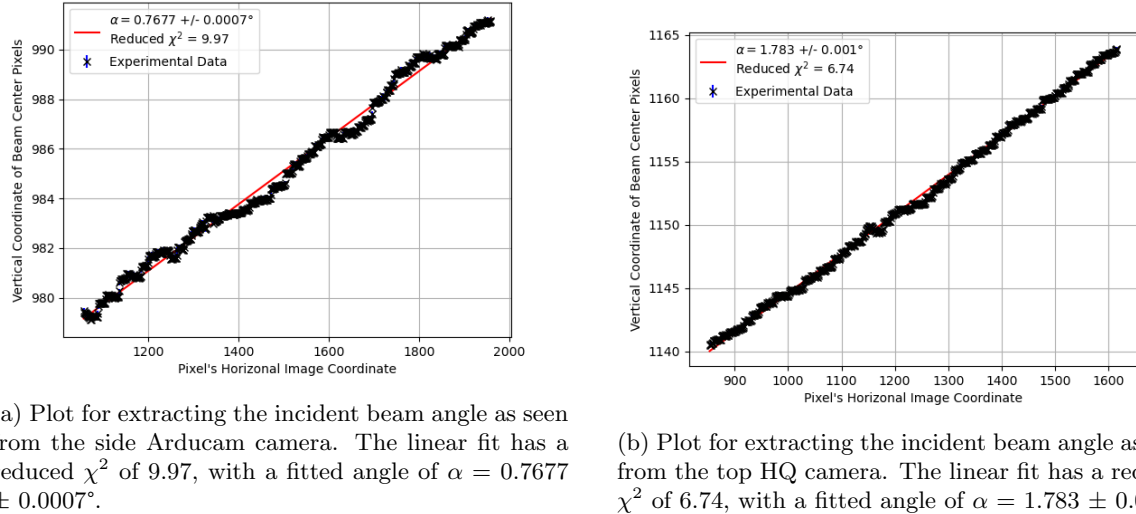


Figure 8

Using the beam angle extracted from a camera's perspective, an OpenCV method was applied for rotating the image such that the beamline would be horizontal across the image. Then, the analysis above was repeated, where now we could be more confident that we are correctly fitting Gaussians transverse to the beamline. An example which quantifies the improvement is that, for the 150 MeV beam run discussed throughout, the largest reduced χ^2 of a Gaussian fit decreased from 72 to 56.

In the newly rotated images, we spanned all pixel columns enclosed by the ROI, summing the total pixel brightness within each column and plotted the result as a function of horizontal pixels moved across the image. As can be seen in Figures 9a and 9b, the on-axis scintillation light distribution reflects the Bragg curve for proton LET over penetration depth. The Python library Pybragg [18] can be used to fit the Bortfeld model to these distributions. Then, the horizontal pixel value associated with the fitted curve's peak was defined as the horizontal component of the Bragg peak's image coordinate. Note that this could be specified to sub-pixel precision and thus it needed to be rounded to the nearest whole pixel in order to map the horizontal coordinate to an associated Gaussian beam profile. That profile is required because the vertical component of the Bragg peak coordinate was defined as the pixel with the profile's fitted centre. The latter was also specified to sub-pixel precision. Finally, the identified Bragg peak image coordinate could have an inverse rotation matrix applied, converting it back into the coordinates

of the raw image. This step was essential as the homography we constructed was built for the original image coordinates.

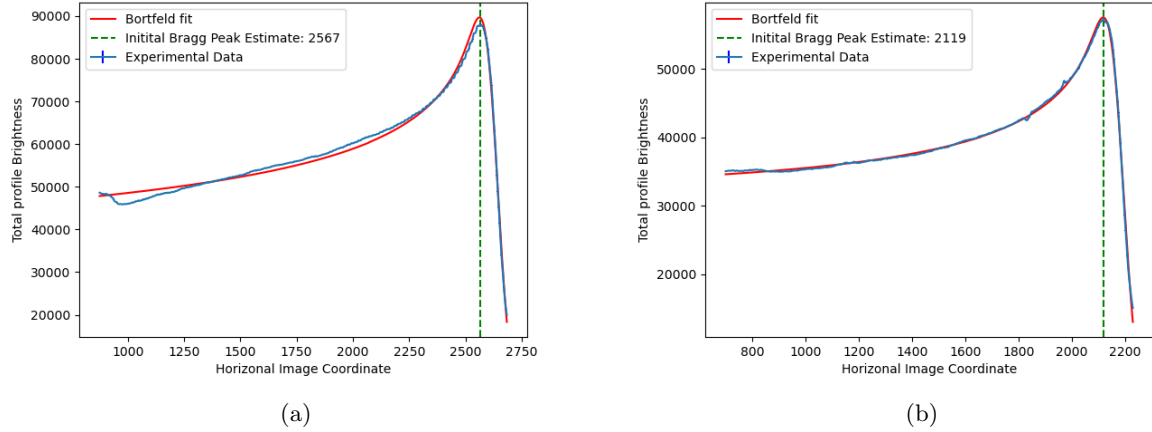


Figure 9: (a) and (b) show the Bortfeld model fitted to the 150 MeV on-axis scintillation distribution extracted from side Arducam/top HQ camera images respectively. The green dashed lines show the horizontal image coordinates that would be inferred for the Bragg peak from the maximum absolute brightness of a fitted Gaussian profile.

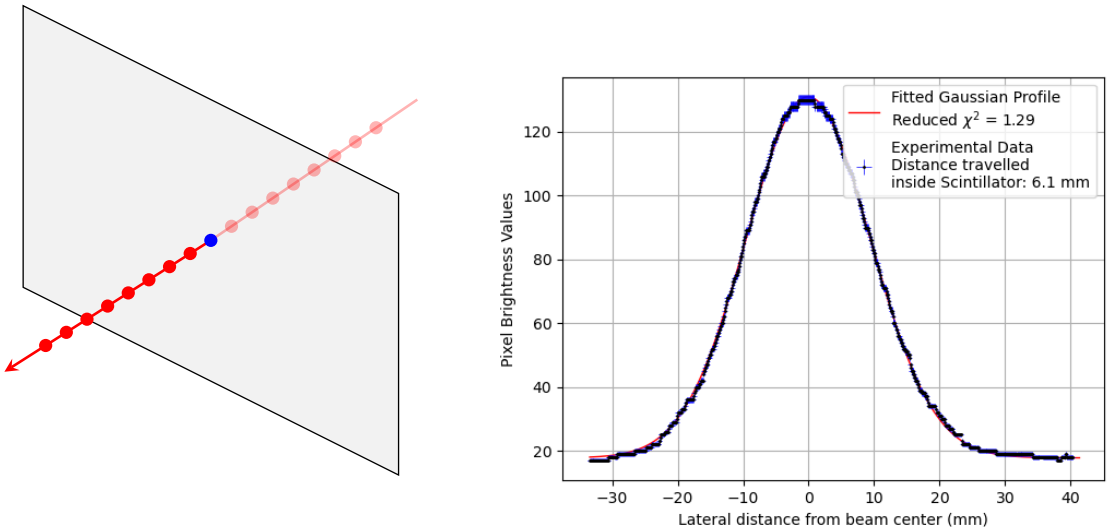
7.2 3D Pinpointing of the Bragg Peak

For each beam run, the procedure for Bragg peak pixel determination was implemented for both the side-mounted Arducam camera and the top-mounted HQ camera. Each could have its line of possible positions interpolated using our homographies, and therefore the line-intersection method could be executed to 3D pinpoint the beam’s Bragg peak. As an example, for the 150 MeV beam run, the distance of closest approach between the two interpolated lines is 0.4 mm, and the Bragg peak’s physical position in our coordinate system is $(16.9, 43.5, 142.7) \pm (0.4, 0.1, 0.3)$ mm. For a given beam run, the 3D Bragg peak position could be combined with the two incident beam angles we extracted to build an estimated vector equation for the beam’s path through physical space.

From here onwards, only data from the side Arducam camera was required. Using the Gaussians fitted to the rotated image, the 2D coordinates of each Gaussian centre can be constructed and rotated back into the coordinate system of the original image. The two homographies prepared for this camera can be used yet again to project each beam centre image coordinate onto the calibrated world planes, and a line of possible physical positions in which that light emanates from can be interpolated. Each of these lines can have the intersection method applied between them and the constructed line equation for the beam’s path. Therefore, the 3D positions of these beam centres, each a different length along the beam axis, can be determined so as to produce a 3D reconstruction of the proton beam’s central line. Two further analyses are developed from this data.

7.3 Scintillation Distributions in Physical Distance Units

The 3D reconstruction of the beam allows the conversion of the lateral scintillation light distribution, expressed above within pixel units, into physical units. The setup here is given in Figure 10a, where the red line represents the beam centre vector equation and the numerous dots along it symbolise the 3D reconstructed beam centre positions. Say a given Gaussian beam profile is deemed of interest, you can build the 2D coordinates of the full profile within the rotated image to then transform them back into the raw image’s coordinate system. The centre of this Gaussian has its 3D position determined already, and so one can define a plane, whose normal is the beam’s direction vector, that contains said beam centre. Given that the scintillation light distribution is Gaussian transverse to the beam-axis, we assert the physical positions of each image coordinate within the profile must lie upon this plane. The



(a) A diagram showing the position/orientation of the plane to be used in the plane-line intersection method when converting a Gaussian beam profile into physical distance units. The centre of the profile is marked in blue.

(b) An example of a Gaussian beam profile, as seen by the side Arducam camera, expressed in terms of physical distance units. This profile is extracted from the beam after travelling 6.1 mm inside the scintillator, and the fit has a reduced χ^2 of 1.29. Both horizontal and vertical error bars are plotted.

Figure 10

lines interpolated via homographies for each image coordinate can be intersected with the plane to 3D pinpoint each contribution to the observed Gaussian distribution. Finally, computing the Euclidean distances between these and the beam's centre completes the conversion of the Gaussian plots into physical distance units. Such a Gaussian profile is depicted in Figure 10b.

Unfortunately, the TOPAS simulations performed this semester do not provide a Gaussian beam profile width, although they could possibly be extended to do so next semester. Again, this semester has centred on developing the first version of an automated data analysis pipeline, in preparation for its subsequent integration into the GUI. That being said, Dr Michael Taylor, a member of the group who undertakes research at the Christie Hospital, provided some rough beam width parameters; the Gaussian-shaped 150 MeV beam has a measured σ parameter of 7.98 mm (to two decimal places). Unfortunately, this was provided without an associated uncertainty. The fitted σ parameter for Figure 10b is 9.48 ± 0.01 mm. An explanation for the discrepancy is that we can only extract Gaussian profiles some distance into the scintillator since reflected scintillation light from the anterior face washes out the underlying Gaussian distribution in that region. For figure 10b, the beam has travelled around 6.1 mm into the scintillator, hence the Gaussian beam is expected to have broadened due to multi-coulomb scattering. Of course, more concrete study into the beam width would be needed before we can confirm the accuracy of the method described for conversion to physical distance units.

The second analysis possible because of the beam's 3D reconstruction is the conversion of the on-axis scintillation light distribution into physical units. Using the incident beam angles and 3D Bragg peak position, we can extrapolate the beam's central line back, beyond the region of interest in which we restricted our analysis, in order to determine the beam's incident position upon the anterior face of the scintillator. With this incident position, we can explicitly calculate the penetration depth associated with the Bragg peak as a Euclidean distance traversed within the scintillator; the method employed last semester assumed normal incidence and thus took the Bragg peak's depth as simply the on-axis displacement. The total brightness across each beam profile could be plotted as a function of the penetration depth determined for the profile centres. These curves are plotted for $\{130, 150, 160, 170, 180\}$ MeV beam energies within Figure 11a. Each has their Bragg peak brightness normalised to unity, and their associated Bragg peak depths are included in the legend.

These can be compared to Bragg curves extracted from Monte-Carlo simulations of our experimental

setup, as depicted in Figure 11b. These curves are also normalised to unity, which was necessary since the experimental plots have intensity values along the vertical axis, whereas the simulated ones have the linear energy transfer instead. The nature of these simulations will be described further in Section 8. A difference in Bragg peak width between the experimental and simulated plots can be seen. The occurrence of Spread-Out Bragg Peaks (SOBPs) arises when the proton beam undergoing interactions does not begin mono-energetic; within the simulations, the energy of incident protons was drawn from a Gaussian distribution of width 1 MeV. The experimental source of such an energy spread could be the statistical nature of proton interactions within the ESS, however the overall spread in the Christie's proton beam may be larger than this. If so, the simulated Bragg peak width is underestimated. Additionally, I have mentioned how the analogue gains used have likely lead to some amount of saturation around the Bragg peaks in all beam runs. As a consequence, what would be a sharp peak is washed out due to the surrounding distribution increasing in brightness while the peak brightness remains invariant.

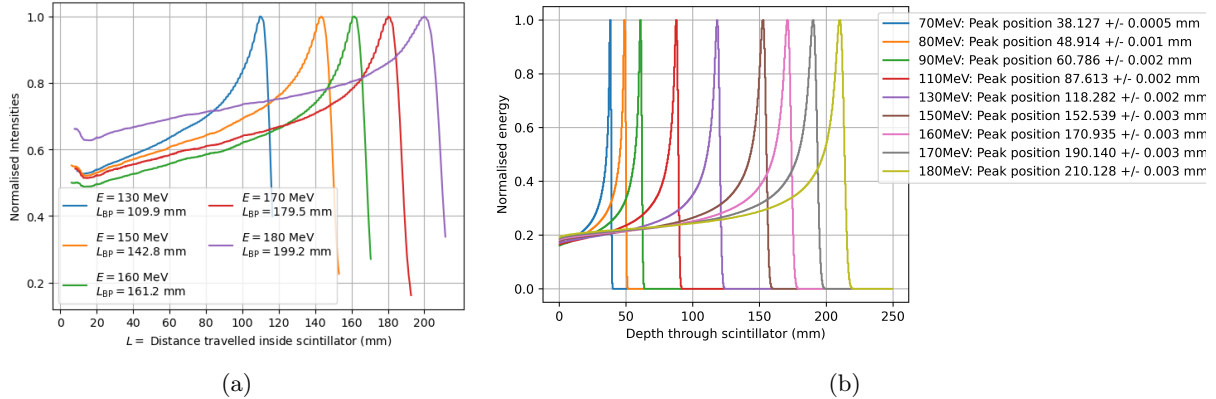


Figure 11: (a) The normalised scintillation light Bragg curves for 5 beam energies spanning the 130-180 MeV domain. Depths have been cast from pixel units into millimetres. The L_{BP} labels in the legend denote each curves associated Bragg peak depth. (b) Normalised TOPAS Simulated Bragg curves spanning the 70-180 MeV domain.

8 TOPAS Simulations

In the final few weeks of the project, Robin created some Monte-Carlo simulations for our experimental setup using TOPAS, a piece of software built on top of Geant4 for application to medical physics. These serve as a point of comparison between our experimental analysis and that predicted by theory. The scintillator's dimensions, density and material are all inputted simulation parameters, however one aspect of the setup we are yet to confidently implement is the distance travelled through air after exiting the beamline's nozzle before incidence upon the scintillator. Given that we do not have access to a value for this distance, we settled upon a value of 1.5 m based upon an image we had of the setup. Next semester, we want to measure this distance to ensure it is incorporated into the simulations accurately. For each simulated beam energy, 10,000 protons were made incident upon the scintillator. Then, the scintillator was decomposed into cubic bins of side length 0.5 mm and the proton LET deposited into each was recorded. Summing the energy in all bins of a given on-axis depth collapses the 3D binning into a 1D one, which could then be plotted as done in Figure 11b.

8.1 Comparison of Experimental and Simulated Bragg Peak Depths

The simulated Bragg peak depths are compared to those extracted from our image analysis in Table 3. Despite the more advanced analysis performed this semester, we have arrived at a similar conclusion to the previous students. That is, our analysis is inconsistent with the nominal energy the protons are said to leave the Christie's energy selection system (ESS) with. However, as their results also implied, all our Bragg peak depths would be consistent with the simulations if the centre of the beam's energy

Beam Energy (MeV)	Simulated Bragg Peak Depth (mm)	Experimental Bragg Peak Depth (mm)
127	110.90 ± 0.02	
130	115.58 ± 0.02	109.9 ± 0.7
133	120.46 ± 0.02	
147	143.85 ± 0.02	
150	149.20 ± 0.02	142.8 ± 0.7
153	154.44 ± 0.02	
157	161.65 ± 0.03	
160	167.18 ± 0.03	161.2 ± 0.7
163	172.68 ± 0.03	
167	180.19 ± 0.03	
170	185.95 ± 0.03	179.5 ± 0.7
173	191.71 ± 0.03	
177	199.58 ± 0.03	
180	205.68 ± 0.03	199.2 ± 0.7
183	211.56 ± 0.03	

Table 3: A comparison of the Bragg peak depths determined by our experimental analysis of the images, as well as those taken from TOPAS Monte-Carlo simulations of our scintillator setup. Consistency is only achieved for the proposed scenario in which the simulated beam energies are 3 MeV lower than whatever nominal energy is associated with the experimental beam run.

distribution was 3 MeV lower. Note, the choice of estimated air-to-scintillator distance acts to shift the entire beam energy distribution. Given that this distance is currently only approximated, any residuals we see between the experimentally determined depths and simulated ones will be subject to change once the distance of the air gap is actually measured. It's possible that after exiting the ESS, there are additional energy losses during the beam's transport to the scintillator, for example as the beam is focussed by the quadrupole magnets. Good estimates for these energy losses may be hard to quantify, however the beamline's nozzle features a Multi-Strip Ionisation Chamber (MSIC), used to measure the proton energies at the end of the beam's preparation. For our purposes, it would be more valuable if we had access to the energy measured here, since we can then simulate the proton's interactions within air and inside the scintillator using TOPAS. Doing so would bypass the need to quantify the energy losses introduced during beam transport prior to the nozzle and may elucidate why both analyses applied to these images have concluded the same systematic error in nominal beam energy.

Another nuance which may contribute to the the residuals between simulated and observed Bragg peak depths is the discrepancy between the focus we set for the top mounted HQ camera when taking calibration images and those used last semester at the Christie Hospital. As mentioned, the HQ cameras are focussed manually, however both the distortion calibration and the building of homographies are focus-dependent processes. Given that during our method we are applying two homographies to a single image, a camera's focus had to be constant across the separate images of front and back calibration world planes; therefore, the focal plane was set approximately in-between these two planes. We cannot be sure what focus the HQ cameras had for the images of scintillation light used, therefore, depending on how significant homographies depend on focus settings, this variation may skew the validity of physical positions obtained through our homographies.

8.2 Discussion of our Sources of Error

The error propagation for this analysis was tedious, with the initial sources of error having been propagated through 3 “intersection methods” (3D Bragg peak pinpointing, beam centre pinpointing and the plane-line intersection method) for determination of the error on lateral distances across beam profiles like that seen in Figure 10b. Besides a possible systematic error in the simulated beam energies, there are three key sources of error which propagate throughout our analysis. These are:

1. Measurements necessary for translation from the coordinate systems of calibration planes into the coordinate system defined for the box. These were measured with digital calipers (although a ruler was used in one instance).
2. The choice of grid spacing size in the calibration patterns employed.
3. The precision in which the pixel containing the Bragg peak, within the averaged image from each camera perspective, can be identified.

The second and third contributions are grouped together as the error introduced by the homographies. I took the initial calibration images for building our homographies, which used a chessboard pattern with 10 mm spacings. Towards the end of the semester, Robin explored how the accuracy of positions determined via homography varies with the spacing between the chessboard tiles; he showed that a finer chessboard calibration reduced the residuals between points measured with a ruler and the positions inferred by a homography. As a result, he decided to improve our calibration by imaging chessboards with 2 mm spacing. However, due to inefficiencies in the code implemented to compute the error on homography cannot handle such a large number of chessboard corners. Therefore, we had to settle for the poorer calibration images for the final results of our analysis which we had not anticipated. Next semester, we need to adapt the code to unlock the potential for more precise positions determination via homographies.

As can be seen in table 3, after rounding the error in our experimental Bragg peak depths one decimal place, it is persistently 0.7 mm. The invariance of the error indicates that it is constant across all image sets; the error introduced by shifting between coordinate systems satisfies this property.

In the case of the original calibration images, the top HQ camera’s calibration pattern had one of the shifts between coordinate systems measured with a ruler. This introduced a 0.5 mm uncertainty in position measurements. When these measurements were made with digital calipers, they had an associated 0.1 mm uncertainty. We saw the error in homography rarely reach 0.1 mm, instead staying around 0.05 mm on average. That being said, the error introduced by the homography and that introduced by measurements with calipers are of comparable magnitude. Despite my computer continually crashing when attempting to use the new set of calibration images, Robin managed to compute the Bragg peak depth for the 150 MeV beam run prior to any crashes: its value was 144.1 ± 0.2 mm. Note that this depth has moved closer to the depth obtained in the 150 MeV TOPAS simulation. The reduced error is because these calibrations had a much finer chessboard pattern and all shifts were measured with calipers. Clearly, its would have benefitted our analysis if these higher quality calibrations could have been used throughout.

9 Extensions for Semester Two

Despite the multitude of automation introduced to image analysis this semester, there are still improvements to be made. For example, a system for the automated selection of appropriate regions of interest within all image datasets needs devising. Its possible that the Canny edge detection algorithm, or some alternative algorithm, would be capable of detecting the edges of the beam’s penumbra, and some energy-dependent margin could be added to the beam’s edges to construct regions of interest. Another approach could see all the contours identified by the Canny edge detection algorithm passed into an artificial neural network to be trained to build appropriate regions of interest through those we have had to manually define for each image set this semester. Additionally, the series of test runs performed to determine optimum analogue gains could be automated. By accounting for the relationship between gain and exposure time, a large number of gain settings could be quickly tested if we take many images, each with low exposure time. Then, scaling the pixel brightnesses observed to reflect the exposure time

of the main beam run, we could select the highest gain tested which would not saturate the Bragg peak.

Another improvement would be introducing data from additional side/top mounted cameras within the box; then, the weighted line-intersection method, described in Section 6.3.1, could be used between all camera pairings, increasing the precision of 3D pinpointed positions further. The application of the intersection methods would likely need parallelising however, given that our full analysis takes around two minutes to run when just two cameras are used. We are yet to identify how the on-axis camera data can be incorporated into our analyses.

Of course, the overarching goal of Semester Two will be the completion of a robustly tested, user-friendly GUI that abstracts many aspects of the calibration/data analysis pipelines we developed this semester. We intend for the basic HTML structure of the prototype to be replaced by the React framework Next.js, allowing the quick development of a more sophisticated frontend experience for potential users of the software. An essential aspect of the GUI will be a built-in user manual, for both documenting the backend analysis and explaining how a user should perform camera calibrations through the interface.

10 Conclusion

This semester has been critical in the early stages of the GUI's development. Given that the previous analysis procedure relied on various pieces of software and manual user input, it was imperative that we develop the Python-coded pipeline that has been implemented thus far. Additionally, we no longer assume the brightest pixel is an optimal way of determining the image coordinate associated with the Bragg peak, and the new method allows all scintillation light distributions to be cast into functions of the physical distances propagated inside the scintillator. Next semester, we will build the tools needed to embed calibration preparation into the GUI, in addition to providing a diverse set of features which allow users to customise how they would like to analyse the data within their images.

The dominant source of uncertainty introduced by our procedure was unfortunately the ruler measurement made for shifting between the coordinate system of a calibration plane and the box's coordinate system. Next semester, no such error would be present, and we will strive to allow finer calibration patterns to be used, further reducing the error introduced by the homographies created. At the same time, our experimental results disagree with our nominal beam energy simulations just as was observed by the previous group of students. This implies some systematic deviation may exist between the beam energy leaving the nozzle and that upon its exit from the ESS. Perhaps the process of focussing the beam prior to the nozzle is somewhat dissipative. These issues need addressing next semester if we are to confidently say that this apparatus can accurately and precisely measure Bragg peak depths inside a scintillator.

References

- [1] B. Liu, H. Zhou, L. Tan, K. T. H. Siu, and X.-Y. Guan, “Exploring treatment options in cancer: Tumor treatment strategies,” en, *Signal Transduction and Targeted Therapy*, vol. 9, no. 1, p. 175, Jul. 2024, ISSN: 2059-3635. DOI: 10.1038/s41392-024-01856-7. [Online]. Available: <https://www.nature.com/articles/s41392-024-01856-7> (visited on 12/11/2024).
- [2] R. R. Wilson, “Radiological Use of Fast Protons,” en, *Radiology*, vol. 47, no. 5, pp. 487–491, Nov. 1946, ISSN: 0033-8419, 1527-1315. DOI: 10.1148/47.5.487. [Online]. Available: <http://pubs.rsna.org/doi/10.1148/47.5.487> (visited on 12/11/2024).
- [3] J. D. Aylward, N Henthorn, S Manger, *et al.*, “Characterisation of the UK high energy proton research beamline for high and ultra-high dose rate (FLASH) irradiation,” *Biomedical Physics & Engineering Express*, vol. 9, no. 5, p. 055 032, Sep. 2023, ISSN: 2057-1976. DOI: 10.1088/2057-1976/acef25. [Online]. Available: <https://iopscience.iop.org/article/10.1088/2057-1976/acef25> (visited on 12/09/2024).

- [4] H. M. Kooy, B. M. Clasie, H.-M. Lu, *et al.*, “A Case Study in Proton Pencil-Beam Scanning Delivery,” en, *International Journal of Radiation Oncology*Biology*Physics*, vol. 76, no. 2, pp. 624–630, Feb. 2010, ISSN: 03603016. DOI: 10.1016/j.ijrobp.2009.06.065. [Online]. Available: <https://linkinghub.elsevier.com/retrieve/pii/S0360301609010116> (visited on 12/09/2024).
- [5] “Accelerating the development of proton beam therapy,” en, The Cockcroft Institute of Accelerator Science and Technology, Tech. Rep. [Online]. Available: <https://www.cockcroft.ac.uk/2022/06/08/accelerating-the-development-of-proton-beam-therapy/> (visited on 12/11/2024).
- [6] *PDG Atomic and nuclear properties of polyvinyltoluene*. [Online]. Available: <https://pdg.lbl.gov/2014/AtomicNuclearProperties/HTML/polyvinyltoluene.html> (visited on 12/05/2024).
- [7] H. Nakamura, Y. Shirakawa, N. Sato, *et al.*, “Optical characteristics of pure poly (vinyltoluene) for scintillation applications,” en, *Nuclear Instruments and Methods in Physics Research Section A: Accelerators, Spectrometers, Detectors and Associated Equipment*, vol. 770, pp. 131–134, Jan. 2015, ISSN: 01689002. DOI: 10.1016/j.nima.2014.10.018. [Online]. Available: <https://linkinghub.elsevier.com/retrieve/pii/S0168900214011656> (visited on 12/09/2024).
- [8] W. Frass, *Oxford Physics - Passage of Particles Through Matter*, en, 2009. [Online]. Available: <https://www2.physics.ox.ac.uk/sites/default/files/Passage.pdf> (visited on 12/12/2024).
- [9] T. Bortfeld and W. Schlegel, “An analytical approximation of depth - dose distributions for therapeutic proton beams,” *Physics in Medicine and Biology*, vol. 41, no. 8, pp. 1331–1339, Aug. 1996, ISSN: 0031-9155, 1361-6560. DOI: 10.1088/0031-9155/41/8/006. [Online]. Available: <https://iopscience.iop.org/article/10.1088/0031-9155/41/8/006> (visited on 12/09/2024).
- [10] V. L. Highland, “Some practical remarks on multiple scattering,” en, *Nuclear Instruments and Methods*, vol. 129, no. 2, pp. 497–499, Nov. 1975, ISSN: 0029554X. DOI: 10.1016/0029-554X(75)90743-0. [Online]. Available: <https://linkinghub.elsevier.com/retrieve/pii/0029554X75907430> (visited on 12/11/2024).
- [11] *Arducam IMX519 Camera Specification*, en. [Online]. Available: <https://www.arducam.com/product/imx519-autofocus-camera-module-for-raspberry-pi-arducam-b0371/> (visited on 12/05/2024).
- [12] A. Phillips, “Investigating Bragg Peak Characteristics using Raspberry Pi Cameras,” University of Manchester, Semester Two Report, Dec. 2024. (visited on 12/09/2024).
- [13] *Calib.io Pattern Generator*, en. [Online]. Available: <https://calib.io/pages/camera-calibration-pattern-generator> (visited on 12/11/2024).
- [14] A. Criminisi, I. Reid, and A. Zisserman, “A plane measuring device,” en, *Image and Vision Computing*, vol. 17, no. 8, pp. 625–634, Jun. 1999, ISSN: 02628856. DOI: 10.1016/S0262-8856(98)00183-8. [Online]. Available: <https://linkinghub.elsevier.com/retrieve/pii/S0262885698001838> (visited on 12/09/2024).
- [15] R. Hartley and A. Zisserman, *Multiple view geometry in computer vision*, eng, 2. edition, 17.printing. Cambridge: Cambridge Univ. Press, 2018, ISBN: 978-0-521-54051-3.
- [16] *Company Profile - An introduction to the LEGO Group*, 2010. [Online]. Available: <https://web.archive.org/web/20121209100137/http://cache.lego.com/upload/contentTemplating/AboutUsFactsAndFiguresContent/otherfiles/download98E142631E71927FDD52304C1C0F1685.pdf> (visited on 11/14/2024).
- [17] C. Bartneck, *LEGO Brick Dimensions and Measurements*, Mar. 2019. [Online]. Available: <https://www.bartneck.de/wp-content/uploads/2019/03/LEGO-Brick-Dimensions-Measurements.pdf> (visited on 11/14/2024).
- [18] *Pybragg Python Package*. [Online]. Available: <https://github.com/flome/pybragg> (visited on 12/06/2024).